

Controlling the Electronic Interface Properties in Polymer–Fullerene Bulk Heterojunction Solar Cells

T. Stubhan, N. Wolf, J. Manara, V. Dyakonov, and C.J. Brabec

Contents

1 Introduction	294
1.1 Reference Solar Cells.....	295
1.2 Fundamentals and Mechanisms.....	295
1.3 Processing of Interface Materials.....	298
1.4 Interface Modification Layers.....	301
1.5 Stability of Interface Materials.....	307
1.6 Summary.....	308
References	309

Abstract This work covers the use of solution-processed metal oxides as interface layers for organic solar cells. To study the interface properties, intrinsic and Al-doped ZnO_x were chosen as reference systems. From the class of n-type metal oxides, ZnO_x was chosen because it can be doped when it is solution processed.

T. Stubhan (✉)

Materials for Electronics and Energy Technology (i-MEET), Friedrich-Alexander-Universität
Erlangen-Nürnberg, Martensstrasse 7, 91058 Erlangen, Germany
e-mail: tobias.stubhan@fau.de

N. Wolf • J. Manara • V. Dyakonov

Bavarian Center for Applied Energy Research (ZAE Bayern), Am Galgenberg 87, 97074
Würzburg, Germany
e-mail: jochen.manara@zae-bayern.de

C.J Brabec

Materials for Electronics and Energy Technology (i-MEET), Friedrich-Alexander-Universität
Erlangen-Nürnberg, Martensstrasse 7, 91058 Erlangen, Germany

Bavarian Center for Applied Energy Research (ZAE Bayern), Haberstr. 2a, 91058 Erlangen,
Germany

Furthermore, the influence of thin modification layers applied on top of the metal oxides is investigated.

Keywords Aluminum-doped zinc oxide • Barium hydroxide • Charge transport in nanoparticulate films • Conjugated polyelectrolyte • Device structure • Diketopyrrolopyrrole-quinoxaline • Doped zinc oxide • Electronic surface properties • Energy diagram • Energy-level diagrams • EQE spectra • Interface layers for organic solar cells • Interface layers • Interface modification layers • Inverted organic solar cells • J - V characteristics • Low temperature • Molybdenum oxide • Mott–Schottky capacitance • Oxygen • P3HT • PCDTBT • Phosphonic acid anchored fullerene SAM • Polyvinylpyrrolidone • Poole–Frenkel effect • Reference solar cells • SAM modification • Stability of interface materials • Stabilization of AZO nanoparticles • Summary • Thickness dependence • Trioxadecanoic acid • Water • Zinc oxide

1 Introduction

Organic solar cells have been processed in two different geometries: (1) in the inverted geometry, where the ZnO layer is directly processed on the transparent conducting oxide electrode as well as (2) in the normal cell structure, where the ZnO is deposited on top of the semiconductor and beneath the top cathode. This was possible because in addition to the classical sol-gel-processed ZnO_x layers we were able to process intrinsic and Al-doped ZnO_x layers via a nanoparticle suspension without high-temperature annealing processes that harm the polymeric active layer. The main objectives were to systematically vary the doping level and to build a correlation between the device functionality and the work function of the interface layer: its conductivity and carrier concentration, respectively.

Finally, these investigations provided valuable insight into the origin of the second diode and surface recombination in organic solar cells. Second diodes are internal diodes in solar cells that are connected in series to the photovoltaic junction and cause a kink in the J - V curve in the fourth quadrant and a delayed opening of the diode in the first quadrant [1].

The main aspect of this work was the development, advancement, design, characterization, and understanding of interface layers for a solution-processed polymer–fullerene solar cell. Although the development of the full solar cell (including the semiconductor, top electrode, and packaging) was not the focus of this work, this research delivered further important input to the architecture and design criteria for the rest of the solar cell's stack.

The first part of this work focused on the development and characterization of solution-processed ZnO at various bulk doping levels. The second part focused on modifying the electronic surface properties of doped and intrinsic ZnO. A description of the work's progress and the results obtained are summarized in the following sections.

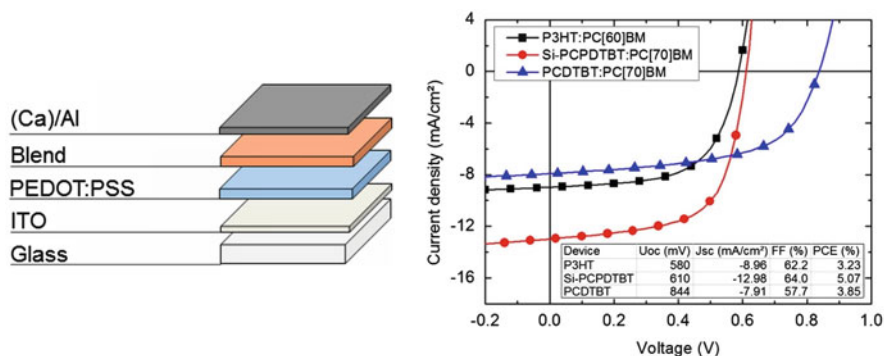


Fig. 1 *Left:* layer stack of the normal architecture solar cells. *Right:* J – V characteristics of the representative polymer solar cells with different donor polymers

1.1 Reference Solar Cells

Reference solar cells were built in the normal architecture. Figure 1 displays representative J – V curves of solar cells and the standard architecture used with different donor polymers in the active layer.

1.2 Fundamentals and Mechanisms

1.2.1 Charge Transport in Nanoparticle Thin Films of ZnO and Aluminum-Doped ZnO

According to the first part of the work package, the synthesis, characterization, and testing of reference materials, namely ZnO, TiO_x, and a first aluminum-doped ZnO (AZO) precursor according to known routes taken from the literature [2–4], started. The lattice and crystallite structure of the materials was investigated through X-ray diffraction measurements. We obtained anatase TiO_x with a crystallite size of 12.5 nm and wurtzite ZnO and AZO with crystallite sizes of 4.2 and 4.0 nm, respectively. A slight shift in the peak of the 002 plane of the AZO in comparison to the ZnO is a sign for interstitial doping. With optical measurements, the transmission and bandgap of the materials were investigated and found to be in a suitable range for a window layer in solar cell applications. The transmission of all materials is over 90% in the visible part of the spectrum. This is a result of the wide optical bandgaps: 3.85 eV for TiO_x, 3.44 eV for ZnO, and 3.34 eV for AZO. Electrical characterization showed conductivities on the order of 10^{−4} S/cm for TiO_x and 10^{−6} S/cm for ZnO, whereas AZO had the highest conductivity, on the order of 10^{−3} S/cm.

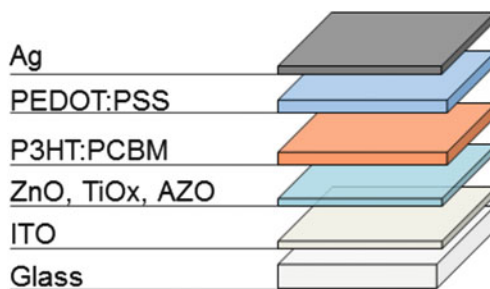


Fig. 2 Layer stack of the investigated inverted polymer solar cells

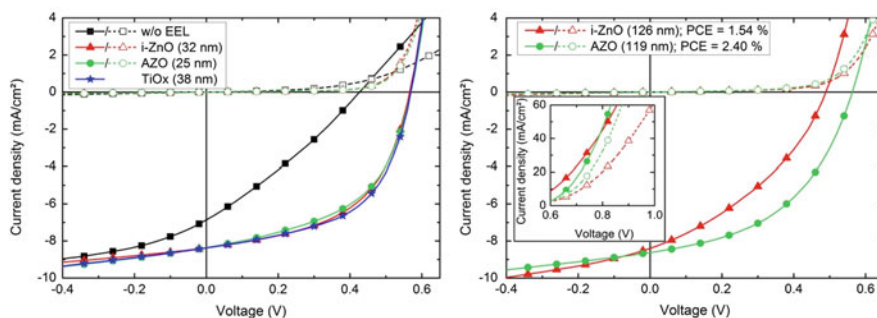


Fig. 3 *Left*: J - V characteristics of the inverted polymer solar cells with thin electron extraction layers. *Right*: J - V characteristics of the inverted polymer solar cells with thick electron extraction layers

Next, these materials were incorporated in inverted polymer solar cells with a usual thickness of a few tens of nanometers (20–40 nm). It was found that all three materials worked comparably and as well as electron extraction layers (EELs) in polymer solar cells (Figs. 2 and 3, right). Interestingly, doped ZnO turned out to be superior to intrinsic ZnO in the thick-film limit, that is, for extraction layers with a thickness of 100 nm and above (Fig. 3, right). The solar cells with thick AZO EELs maintained their performance compared with the thin EELs, but the efficiency of the devices with thick intrinsic ZnO EELs deteriorated (Table 1). Thick and robust films are a prerequisite to reliable large-scale EEL printing.

In subsequent work, the thickness of the interface layer was increased to even 600 nm without limiting the device performance.

As one of our goals was to build more environmentally stable devices, it was necessary to replace the commonly used acidic and hygroscopic PEDOT:PSS as the p-type interlayer, which is known to decrease device lifetimes. Therefore, we developed a solution process to deposit the more stable MoO_3 as the anode interlayer, which yields solar cells with a performance comparable to that of PEDOT:PSS.

Table 1 Key parameters of the inverted solar cells with different materials and thicknesses of the electron extraction layer

	V_{OC} (mV)	J_{SC} (mA/cm ²)	PCE (%)	FF (%)	R_S (Ω /cm ²)	R_{Sh} (k Ω /cm ²)	R (k Ω /cm ²)
w/o EEL	426	−6.86	0.85	29.2	23.6	3.0	0.29
TiO _x	571	−8.38	2.59	54.1	–	–	–
i-ZnO (32 nm)	565	−8.41	2.56	53.9	1.1	6.2	0.59
i-ZnO (126 nm)	486	−8.40	1.54	37.7	3.2	3.1	0.33
AZO (25 nm)	569	−8.36	2.42	50.8	1.1	4.9	0.44
AZO (119 nm)	558	−8.69	2.40	49.4	1.2	3.9	0.50

V_{OC} open-circuit voltage, J_{SC} short-circuit current density, PCE power conversion efficiency, FF fill factor, R_S series resistance, R_{Sh} parallel resistance, R resistance

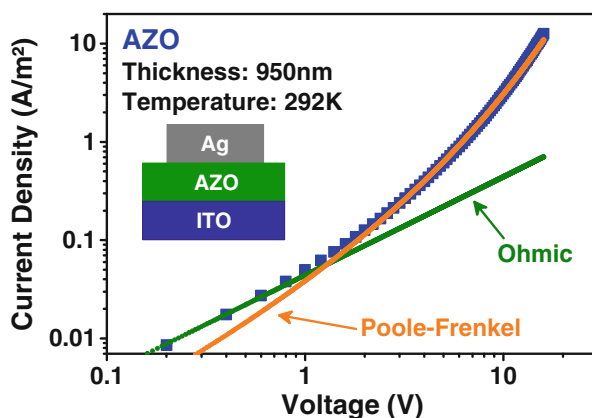


Fig. 4 J – V characteristics of aluminum-doped ZnO in a double-logarithmic plot. Two fit functions demonstrate that the low-voltage data are nicely described by Ohmic behavior, while the high-voltage data follow the Poole–Frenkel effect

1.2.2 Charge Transport in Nanoparticle Thin Films of ZnO and Aluminum-Doped ZnO

To improve our understanding of the above results, we carried out a charge-transport study on intrinsic and doped zinc oxide with commercially available ZnO/AZO dispersions from Nanograde Ltd. While the J – V characteristics at low voltage obey Ohm's law, transport in the high-voltage data regime is controlled by the Poole–Frenkel effect. The occurrence of the Poole–Frenkel effect is related to coulombically bound electrons, which have to overcome a field-dependent barrier to the next nanoparticle. Also, the conduction mechanism was demonstrated to be equivalent for the higher conductive Al-doped ZnO particles, where Al acts as a shallow donor. To the best of our knowledge, this is the first time that the Poole–Frenkel effect was unambiguously demonstrated as the dominant transport mechanism in a nanoparticle thin film (Fig. 4).

1.3 Processing of Interface Materials

Following our work program, the formulation design of doped metal oxide inks was started. As the primary prototype, the metal oxide ZnO was chosen since it has been shown that ZnO [4–8]

- can be processed from solution
- can be doped (e.g., with In, Ag, Ga, Mg, but especially Al)
- has been demonstrated as a functional layer in organic photovoltaic (OPV) cells when it was processed as an intrinsic semiconductor from solution
- has been demonstrated as a functional electrode for organic light-emitting diodes when it was processed from vacuum (atomic layer deposition, sputtering, etc.)

A variety of coating procedures have been well established for many different kinds of applications. In this work, we used sol-gel processes [9] because of their various advantages. Sol-gel precursors are easy to handle in atmospheric conditions, a defined band-doping of the processed materials is possible [10], they are cost-efficient, and they can be deposited by various techniques, including dip coating, spin coating, or several printing and coating processes [11]. There are two different sol-gel processes: the so-called high-temperature and low-temperature paths [12].

In the high-temperature method, the ZnO_x sol is prepared using zinc-acetate-2-hydrate, diethanolamine, and isopropyl alcohol (ISP). Aluminum-nitrate-9-hydrate is added as dopant [13]. The functional layer is formed by annealing the thin-film layer at temperatures over 250 °C [14]. This classic sol-gel process resulted in AZO functional layers with a charge carrier density of $4.2 \times 10^{19} \text{ cm}^{-3}$, a specific resistivity of $3.1 \times 10^{-3} \text{ } \Omega/\text{cm}$, and a transmittance of up to 0.88 at a layer thickness of 1250 nm.

The low-temperature path is based on nanoparticle suspensions [15]. These suspensions consist of crystalline ZnO or AZO nanoparticles with a primary particle size between 15–40 nm. The nanoparticles are redispersed in solvents such as ethanol, diethylene glycol, or ISP and stabilized with surface-modifying agents [e.g., carbon acids such as pentanoic or trioxadecanoic acid (TODS)] [14]. The surface-modifying agents are added to the suspension to prevent aggregation and agglomeration of the nanoparticles. Additionally, an ultrasonic dissolver and stirrer are used for deagglomeration. In addition to the surface-modifying agents, a binder phase is necessary to provide a sufficient mechanical stability of the coating by interconnecting the particles on the one hand and to adhere the coating to the substrate on the other hand [16]. The binder phase may also include functional groups that enable a curing of the coating at temperatures below 130 °C by using, for instance, ultraviolet radiation and photostarter. The state-of-the-art are polymeric binder phases based on glycidoxypropyltrimethoxysilane or methacryloxypropyltrimethoxysilane [17].

The nanoparticles themselves can, for example, be prepared by a surfactant-assisted sol-gel method using zinc nitrate and citric acid as starting materials [18]. A polyesterification reaction due to the Pechini process can also be used for the

preparation of ZnO and AZO powders. This synthesis process is based on the chelation of metal ions by an α -hydroxyl acid such as citric acid in order to form stable homogeneous solutions. The powder can be obtained via calcination [19]. The various processes described were completed by a high-temperature calcination (300 °C) and a subsequent particle surface modification to result in stable suspensions with a particle size below 100 nm. These systems can be processed at low temperatures and are compatible with temperature-sensitive substrates such as polymers.

To date there has been only one paper describing the stabilization of AZO nanoparticles in ethylene glycol [20]. As ethylene glycol affects the performance of the solar cells negatively, it could not be used in our work. We have managed to stabilize AZO nanoparticles with at least four different surface-modifying agents in at least three solvents, respectively, solvent mixtures. Therefore, a series of ZnO solutions has been prepared and was successfully integrated in polymer solar cells.

A solution containing AZO particles, TODS surfactant, and ISP was identified as one candidate for yielding suitable films for solar cell integration. Only 140 °C is necessary to anneal these films, so they can be incorporated onto the temperature-sensitive organic active layer. The electrical functionality of the obtained AZO film was confirmed in standard solar cells with the layer stack displayed in Fig. 5 (left). The J - V characteristics in Fig. 5 (right) show that the AZO forms the electron-selective contact with the proper work function to achieve the expected high open-circuit voltage, V_{OC} . The high fill factor (FF) shows the good quality of the AZO EEL.

Further investigations have been performed on redispersed AZO nanoparticle solutions with different stabilizers, and we researched mixtures of stabilizers to find a solution with long-term stability and improved properties within organic solar cells.

Stable suspensions in IPS could be prepared with the surfactants TODS and polyvinylpyrrolidone (PVP) as well as with a mixture of TODS and PVP and with acetylacetone (AcAc), 1,4-butanediol, hexamethylenetetramine, and ϵ -

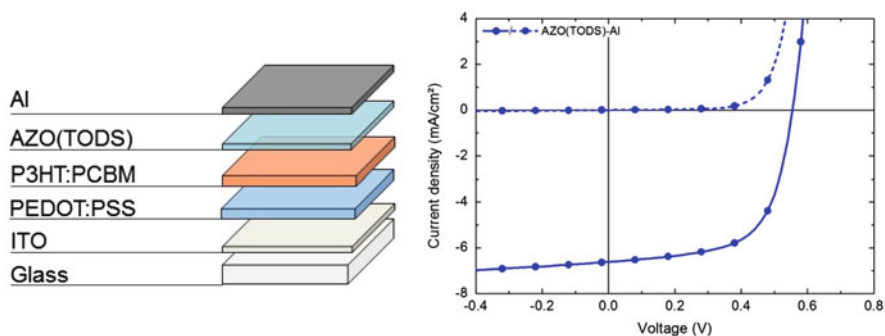


Fig. 5 *Left*: layer stack of the investigated solar cells. *Right*: J - V characteristics of standard solar cells with aluminum-doped ZnO (trioxadecanoic acid) electron extraction layer

Table 2 Hydrodynamic particle sizes of the prepared redispersed AZO nanoparticle solutions using trioxadecanoic acid (TODS), TODS and polyvinylpyrrolidone (PVP), and acetylacetone (AcAc) measured by dynamic light scattering directly after and 3 months after the preparation

Surfactant	TODS (nm)	TODS + PVP (nm)	AcAc (nm)
Particle sizes directly after dispersing	155	145	142
Particle sizes 3 months after dispersing	161	146	155

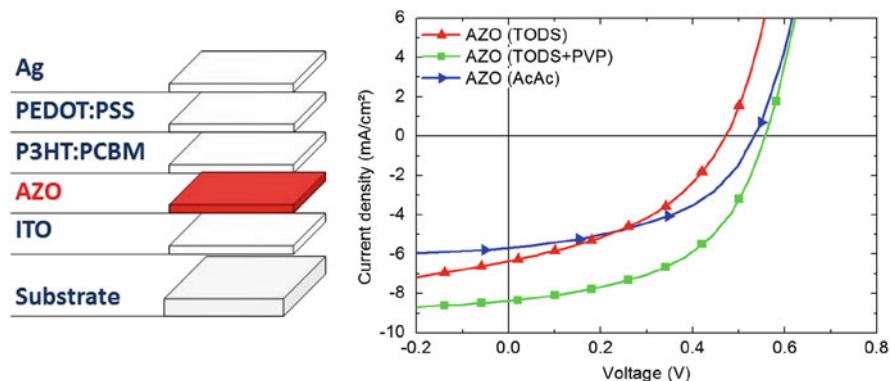


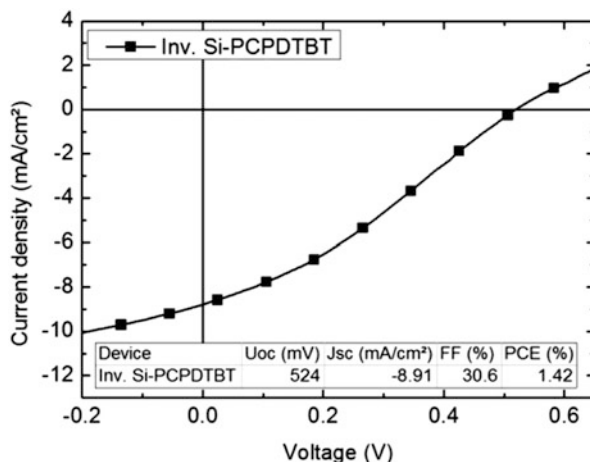
Fig. 6 *Left:* layer stack of inverted polymer–fullerene solar cell with aluminum-doped ZnO (AZO) interface layer. *Right:* J – V characteristics of devices containing AZO interface layers built with trioxadecanoic acid (TODS), TODS and polyvinylpyrrolidone, and acetylacetone nanoparticle suspensions

caprolactone. The smallest particle sizes could be reached by using the surfactants TODS, TODS + PVP, and AcAc, which are shown in Table 2. Usually, the hydrodynamic particle sizes are higher than the primary particle sizes due to agglomeration and aggregation of the primary particles. The particle sizes are similar, which confirms the long-term stability of the prepared AZO nanoparticle solutions.

The surface roughness of the thin films prepared at low temperatures reached values down to 20 nm with an electrical conductivity of up to 10^{-2} S/cm for layers prepared directly after dispersing the AZO nanoparticles as well as for layers prepared with a three-month-old AZO nanoparticle suspension. Finally, inverted polymer–fullerene solar cells have been built with an AZO interface layer using these AZO nanoparticle solutions (Fig. 6, left). The performance of the devices built was found to depend on the surfactant used, with the best obtained with TODS and PVP (Fig. 6, right). The effect can be attributed to a smaller particle size in the dispersion and better layer morphology.

Finally, redispersed AZO nanoparticle solutions with long-term stability have been developed and can successfully be applied to organic solar cells to investigate their properties and improve the performance.

Fig. 7 Inverted solar cell with an aluminum-doped ZnO electron extraction layer and an Si-PCPDTBT:PC₇₀BM active layer (structure similar to Fig. 4)



1.4 Interface Modification Layers

One of the weak points of metal oxide-based EELs frequently discussed is their reliability and reproducibility when processed at low temperature (i.e., at 140 °C). Low processing temperatures may yield incomplete ligand removal and thus result in bad control of the electronic surface properties. For our investigated EEL materials, the performance gap between standard and inverted architecture is small. However, for active layers containing other high-performance donor polymers (e.g., poly[2,6-(4,4-bis-(2-ethylhexyl)dithieno[3,2-*b*:2',3'-*d*]silole)-*alt*-4,7-(2,1,3-benzothiadiazole)] (Si-PCPDTBT); Fig. 7) or small molecules, the gap can be large.

1.4.1 Self-assembled Monolayer Modification

Decorating metal oxides with self-assembled monolayers (SAMs) is one way to achieve predefined surface properties. The experiment depicted in Fig. 8 with the key parameters listed in Table 3 demonstrates how varying the interface properties influences the device performance of inverted solar cells based on poly(3-hexylthiophene-2,5-diyl) (P3HT). The phosphonic acid-anchored aliphatic SAM (SAM-C6) forms a very unfortunate surface on the AZO, which decreases the device performance significantly and inflicts a second diode behavior in the J - V curve. In contrast, the fullerene-functionalized SAMs [SAM(C6-C60) and SAM(C18-C60)] as termination groups for the surface of the doped ZnO films improve the device efficiency [21].

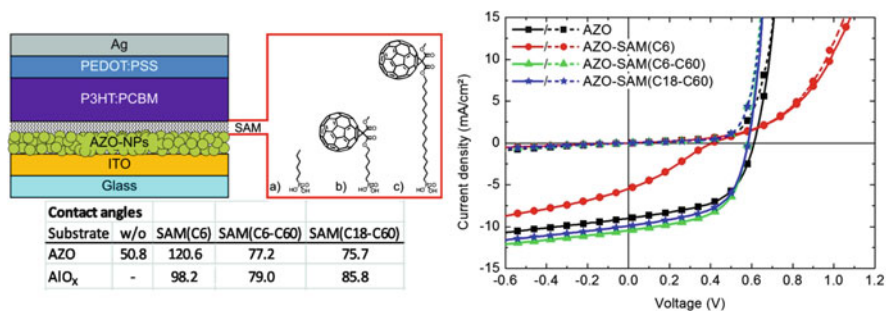


Fig. 8 Left: layer stack of the investigated solar cells including the chemical structure of the self-assembled monolayers (SAMs) and the results of the contact angle measurements to confirm the proper SAM deposition on aluminum-doped ZnO (AZO) and reference AlO_x layers. Right: J - V characteristics of solar cells with SAM-decorated AZO electron extraction layers

Table 3 Key parameters of solar cells with aluminum-doped ZnO electron extraction layers decorated with self-assembled monolayers

	V_{OC} (mV)	J_{SC} (mA/cm ²)	FF (%)	PCE (%)	R_S (Ω /cm ²)	R_p (Ω /cm ²)
AZO	602	-9.23	51.9	2.88	1.2	655
AZO-SAM(C6)	354	-3.94	25.3	0.38	9.5	1011
AZO-SAM(C6-C60)	583	-9.92	57.4	3.32	0.6	1473
AZO-SAM(C18-C60)	584	-9.24	53.5	2.88	0.9	1353

V_{OC} open-circuit voltage, J_{SC} short-circuit current density, PCE power conversion efficiency, FF fill factor, R_S series resistance, R_p polarization resistance

1.4.2 Barium Hydroxide Modification

Inverted organic solar cells with air-stable interface materials and top electrodes and an efficiency of 6.01% are achieved by inserting a barium hydroxide [Ba(OH)₂] layer between the AZO EEL and the active layer. A low-bandgap diketopyrrolopyrrole-quinquethiophene alternating copolymer (pDPP5T-2) and phenyl-C61-butyric acid methyl ester (PC₆₀BM) were chosen as the active layer compounds (Fig. 9). Compared to the control device without Ba(OH)₂, inserting a 10-nm-thick Ba(OH)₂ layer results in an enhanced V_{OC} of 10%, a short-circuit current density, J_{SC} , of 28%, an FF of 28%, and a power conversion efficiency (PCE) of 80% (Fig. 10 and Table 4). Modifying AZO with a solution-processed low-cost Ba(OH)₂ layer increased the efficiency of the inverted device by dominantly reducing the energy barrier for electron extraction from PCBM (see schematic in Fig. 11); consequently, a higher built-in voltage and increased surface charge density are observed (see Fig. 12). The effects of a Ba(OH)₂ layer on the improvement in the device performance stem from the potential surface doping by diffusion of Ba²⁺ ions through the surface of the active layer, the reduced charge recombination, the decreased energy barrier for electron extraction and transport

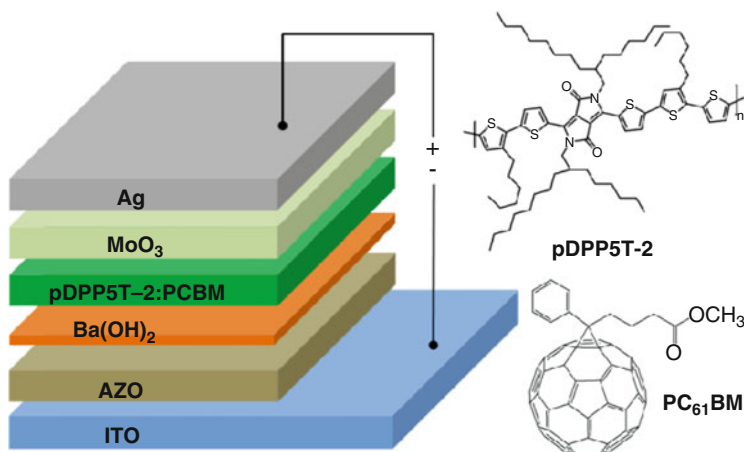


Fig. 9 Schematic of the inverted organic solar cells' structure and chemical structures of the pDPP5T-2 and PC₆₀BM

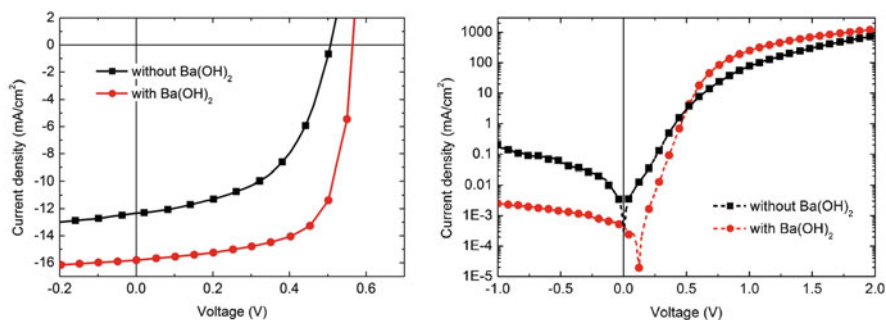


Fig. 10 *Left*: J - V characteristics of inverted organic solar cells without and with the barium hydroxide layer. *Right*: corresponding logarithmic plot of dark J - V characteristics

Table 4 Key values of the J - V characteristics of inverted organic solar cells without and with the Ba(OH)₂ layer

	V_{OC} (V)	J_{SC} (mA/cm ²)	FF (%)	PCE (%)	R_S (Ω /cm ²)	R_{Sh} (k Ω /cm ²)	n	J_0 (mA/cm ²)
Without Ba(OH) ₂	0.50	-12.31	53.90	3.33	1.05	11.58	1.87	1.97×10^{-5}
		-11.78 ^a						
With Ba(OH) ₂	0.55	-15.79	69.18	6.01	0.88	376.41	1.65	4.70×10^{-7}
		-15.19 ^a						

V_{OC} open-circuit voltage, J_{SC} short-circuit current density, FF fill factor, PCE power conversion efficiency, R_S series resistance, R_{Sh} parallel resistance, n , J_0

^aCurrent density values derived from the external quantum efficiency measurement

via inserting an interface dipole layer, and the increased built-in potential from a corresponding increase in the surface charge density [22].

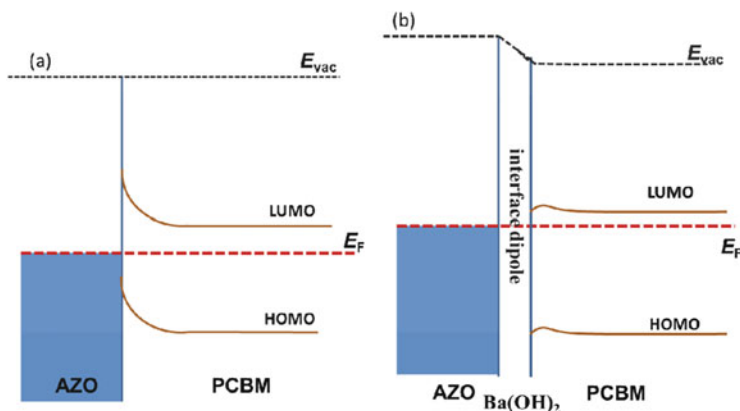


Fig. 11 Schematic energy diagrams for band conditions at the AZO/PCBM junctions (a) without and (b) with barium hydroxide on the AZO layer

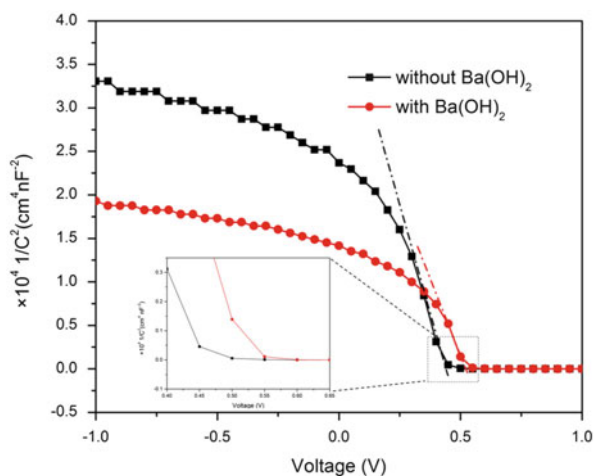


Fig. 12 Mott–Schottky capacitance plots of the voltage data of the device without and with the barium hydroxide layer. Inset: The intercept with voltage axis yields the built-in voltage

1.4.3 Conjugated Polyelectrolyte Modification

The device structure, the molecular structure of poly[3-(6-trimethylammonium-hexyl)thiophene] (P3TMAHT), and the energy levels of the components used in the devices are shown in Fig. 13. Detailed methods for the syntheses of N(Ph-2T-DCN-Et)₃ and P3TMAHT are described in the literature [23, 24]. Through application of the P3TMAHT layer on top of the AZO, the work function of AZO is reduced to from 4.2 to 3.8 eV. Indeed, the increased polarity due to the accumulation of ions

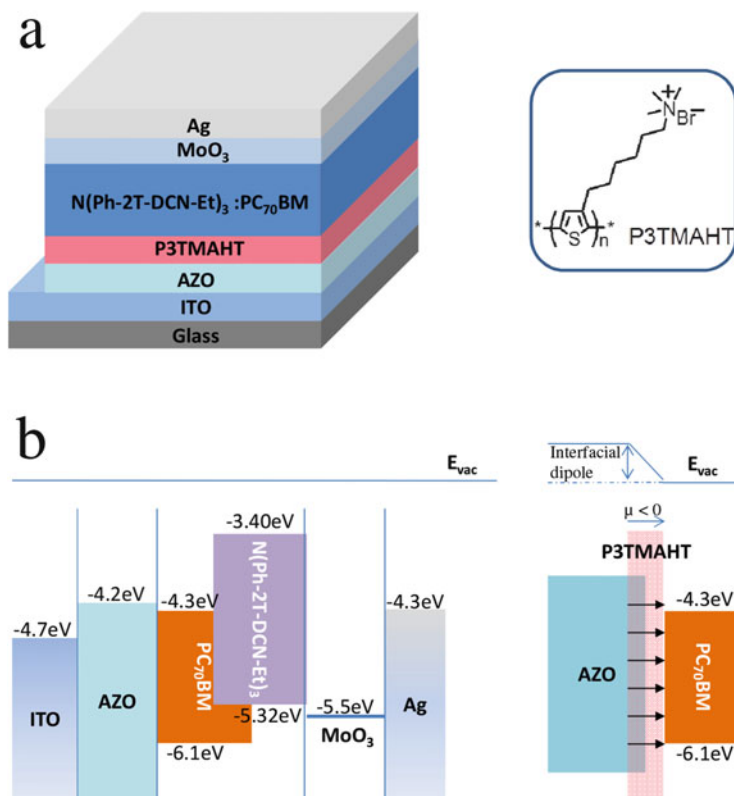
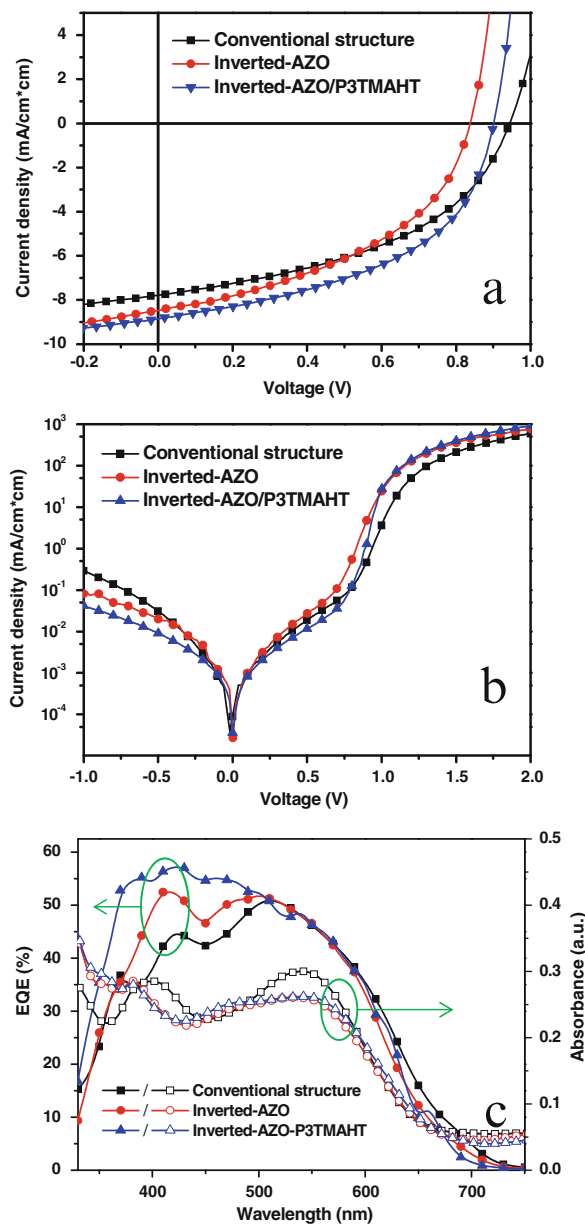


Fig. 13 *Top*: the device structure of the inverted N(Ph-2T-DCN-Et)₃:PC₇₀BM solar cells. Inset shows the molecular structures of P3TMAHT. *Bottom*: schematic energy-level diagrams for flat band conditions at the AZO/(P3TMAHT)/active layer junction with and without the P3TMAHT layer

and the formation of a dipole layer at the interface of AZO is observed as described in the references [25, 26].

The current density vs. voltage (J - V) characteristics of N(Ph-2T-DCN-Et)₃:PC₇₀BM-based conventional [ITO/PEDOT:PSS/N(Ph-2T-DCN-Et)₃:PC₇₀BM/Ca/Ag] and inverted [ITO/AZO/(P3TMAHT)/N(Ph-2T-DCN-Et)₃:PC₇₀BM/MoO₃/Ag] devices under simulated AM 1.5 and in the dark are shown in Fig. 14 (top and middle), respectively. Device parameters are deduced from the J - V characteristics in the light and dark (summarized in Table 5). The reference conventional cells based on N(Ph-2T-DCN-Et)₃:PC[70]BM as active layer have a V_{OC} of 0.939 V, a J_{SC} of 7.79 mA/cm², an FF of 45.9%, and a PCE of 3.36%, while the series resistance (R_S) is 1.29 Ω/cm² and the parallel resistance (R_{Sh}) is 1.84 kΩ/cm². In contrast, the inverted cells based on AZO as the electron-transporting layer show a PCE of 3.17% with a V_{OC} of 0.840 V, a J_{SC} of 8.47 mA/cm², and an FF of 44.5%. The surface recombination, work function

Fig. 14 *Top:* J - V characteristics of the conventional and inverted devices based on various interface layers under the illumination of AM 1.5G, 100 mW/cm^2 . *Middle:* J - V characteristics of the devices in *dark*. *Bottom:* External quantum efficiency spectra of the conventional device and the inverted devices based on various interface layers, and absorption spectra of these blend films of PEDOT/active layer, AZO/active layer, and AZO/P3TMAHT/active layer on the ITO substrates



mismatch, or interface barrier might result in a reduced V_{OC} from 0.939 to 0.840 V, thus resulting in a slightly lower PCE of 3.17%. Consequently, we introduced P3TMAHT as the interface layer on the AZO layer, which facilitates electron injection and transport by reducing the energy barrier between the transparent cathode and active layer. This directly resulted in an increased V_{OC} (from 0.840

Table 5 Performance parameters of N(Ph-2T-DCN-Et)₃:PC₇₀BM solar cells with conventional and inverted structures based on various interface layers

	V_{OC} (V)	J_{SC} (mA/cm ²)	FF (%)	PCE (%)	R_S (Ω /cm ²)	R_P (Ω /cm ²)
Conventional	0.939	7.79	45.9	3.36	1.29	1.84
Inverted-AZO	0.840	8.47	44.5	3.17	1.21	0.85
Inverted-AZO/P3TMAHT	0.898	8.85	49.2	3.91	0.96	2.34

V_{OC} open-circuit voltage, J_{SC} short-circuit current density, FF fill factor, PCE power conversion efficiency, R_S series resistance, R_P polarization resistance

to 0.898 V). In addition, compared with the AZO-based inverted devices, the combination of AZO and the P3TMAHT layer slightly enhanced the J_{SC} (from 8.47 to 8.85 mA/cm²) and FF (from 44.5 to 49.2 %) and thus resulted in a higher PCE of 3.91 %.

Considering the improvement in the J_{SC} , Heeger et al. [27] speculated that the increased built-in potential and internal electric field might help the charge carriers to escape shallow traps and reduce trap-assisted recombination. In addition, Kim et al. [28] thought that the smoother and more hydrophobic surface of the buffer layer (AZO/P3TMAHT layer, as shown in Fig. 14, bottom) improved the compatibility between the organic active layer and the AZO layer and that the better contact induced the enhanced J_{sc} . The external quantum efficiency (EQE) spectra of various devices are shown in Fig. 14 (bottom). The EQE results agree with the J_{SC} of various devices mentioned above.

The improved PCE of the device with the AZO/P3TMAHT layer are also consistent with the higher EQE value (>55 %) exhibited in the PC₇₀BM absorption region between 350–500 nm. Although the absorption spectra of blends on the AZO and AZO/P3TMAHT layer are similar, as shown in Fig. 14 (bottom), the higher EQE values of the AZO/P3TMAHT layer-based device in the PC₇₀BM absorption region prove that AZO/P3TMAHT is more efficiently extracting electrons from PC₇₀BM and thus successfully reduces the recombination.

1.5 Stability of Interface Materials

We synthesized and prepared two different types of Al³⁺-doped ZnO thin transparent films by using a low-cost sol-gel doctor-blade technique. The effect of temperature, adsorption, and diffusion of moisture or moisture vapor on the electrical and optical properties of the films was investigated and correlated to device degradation. The films were placed in a climatic chamber (type C-40/200) for different deposition times. The storage of the samples took place under the following conditions: 40 °C, 90 % relative humidity, 0–140 h. Our results show that the optical properties such as transmittance and bandgap are not influenced by damp-heat testing. Scanning electron microscopy and X-ray diffraction measurements clearly revealed the more amorphous structure of low-temperature AZO thin films

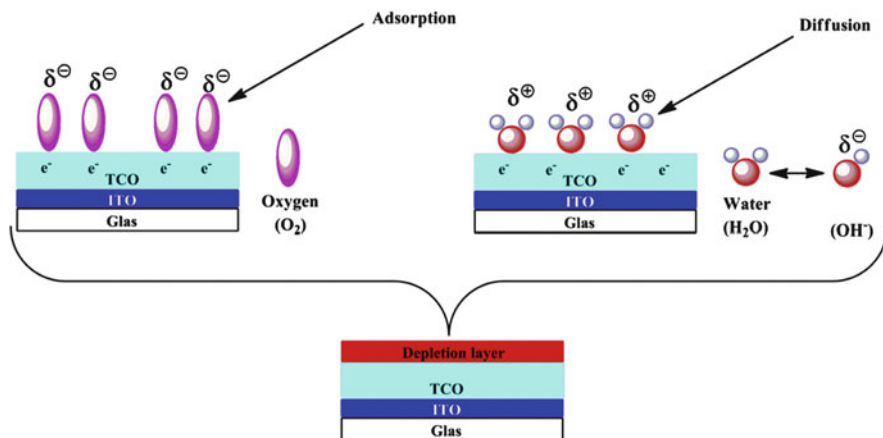


Fig. 15 Schematic view of induced adsorption of oxygen, and diffusion of water or vapor from the ambient atmosphere in the climatic chamber. (Image modified and adapted from [29])

with a nanoporous surface morphology. The analyzed Fourier transform infrared spectra confirmed the impact of both adsorbed oxygen and diffused water on AZO layers, promoting the degradation process (see Fig. 15). The electrical properties of both high- and low-temperature AZO films, that is, work function and conductivity, showed evident degradation upon damp-heat exposure, indicating the strong interaction between the metal surface and the ambient conditions that leads to the formation of a depletion layer. Accelerated device degradation under damp-heat testing underlines the formation of a barrier or depletion layer at the interface, reducing V_{OC} , J_{SC} , and FF. The intrinsic stability of metal oxide-based interlayers as well as that of their nanostructure is an essential criterion for the stability of organic electronic devices. Investigations of different metal oxide surfaces are required to better understand how to further improve the electrical integrity of the surface under damp-heat conditions [30].

1.6 Summary

- Representative solar cells with P3HT, Si-PCPDTBT, and poly[2,6-(4,4-bis(2-ethylhexyl)-4H-cyclopenta[2,1-*b*;3,4-*b'*]dithiophene)-*alt*-4,7(2,1,3-benzothiadiazole)] with power efficiencies between 3–5 % were processed.
- The synthesis, characterization, and benchmarking of the reference materials, namely TiO_x, ZnO, and AZO for EELs in polymer solar cells, were completed. The relationship between material properties and solar cell performance could be established. Applied in thin films, all three materials performed comparably in the solar cells. AZO performed superior to ZnO in the thick film limit. It is

now possible to compare the materials developed in this work to known interface layers.

- A series of AZO formulations with different compositions was developed and the prepared thin films were characterized. A formulation that yields films with suitable properties for the solar cell application could be identified, and the first solar cells that contain these films were built, with promising results.
- Furthermore, the experiments focused on the influence of modification layers on device performance. Three different approaches for surface modifications were applied and investigated:
 - SAMs: PA-anchored aliphatic and fullerene-functionalized SAMs were used as termination groups for doped metal oxide films. The surface properties can be modified over a large interval with a huge impact on device performance.
 - BaOH₂: A thin modification layer of BaOH₂ was applied to AZO. This led to . . . , which improved the device performance of the respective devices by a large margin.
 - CPE: The conductive polyelectrolyte P3MAHT was deposited on top of AZO to improve the performance of inverted small-molecule–based organic solar cells. The P3MAHT reduced the work function, thus enhancing the contact formation to PCBM.
- Additionally, stable redispersed AZO nanoparticle suspensions for a low-temperature coating process that provided long-term stability together with customized electrical properties (such as the electrical conductivity), a small surface roughness, and a high transmittance were developed.
- Conclusions
 - Doping of ZnO allowed us to increase the layer thickness of these interface layers to more than 500 nm without deteriorating device performance.
 - Surface modification has a huge impact on device performance. Many different active layer systems can yield improved performance with surface modifications; however, there is no universal solution. A toolbox based on a suitable doped metal oxide with a variety of modifications proved to be the best approach to adjust the interface properties to the active layers' needs.

Acknowledgment This work is supported by the German Science Foundation (DFG), grant numbers BR 4031/1-1, DY 18/7-1, BR 4031/1-2, and DY 18/7-2.

References

1. Wagenpahl A, Rauh D, Binder M, Deibel C (2010) *Phys Rev B* 82:115306
2. Wang J, Polleux J, Lim J, Dunn B (2007) *J Phys Chem C* 111:14925
3. Alam MJ, Cameron DC (2001) *J Vac Sci Technol A* 19:1642
4. Park Y-S, Park HK, Cho SW, Jeong JA, Choi KH, Kim HK, Lee JY, Cho WJ (2008) *Electrochem Solid-State Lett* 11:J85

5. Huang H-H, Chu SY, Kao PC, Chen YC (2008) *Thin Solid Films* 516(16):5664
6. Yoshida Y, Tanaka S, Hiromitsu I, Fujita Y, Yoshino K (2008) *Jpn J Appl Phys* 47:867
7. Park YR, Nam E, Kim YS (2008) *Jpn J Appl Phys* 47:468
8. Tsai C-L, Lin YJ, Wu PH, Chen SY, Liu DS, Hong HJH, Liu CJ, Chang HC (2007) *J Appl Phys* 101(11):113713
9. Al-Dahoudi N, Aegerter MA (2006) *Thin Solid Films* 502:193–197
10. Dislich H (1986) *J Non-Cryst Solids* 80:115–121
11. Rydzek M, Reidinger M, Arduini-Schuster M, Manara J (2011) *Prog Org Coat* 70:369–375
12. Reidinger M, Rydzek M, Scherdel C, Arduini-Schuster M, Manara J (2009) *Thin Solid Films* 517:3096–3099
13. Rydzek M, Reidinger M, Arduini-Schuster M, Manara J (2012) *Thin Solid Films* 520:4114–4118
14. Rydzek M, Reidinger M, Scherdel C, Arduini-Schuster M, Manara J (2009) *High Temp–High Pressures* 38:277–293
15. Puetz J, Al-Dahoudi N, Aegerter MA (2004) *Adv Eng Mater* 6:733–737
16. Al-Dahoudi N (2003) Dissertation, Universität des Saarlandes
17. Al-Dahoudi N, Aegerter MA (2006) *Thin Solid Films* 520:193
18. Zhang YL, Yang Y, Zhao JH, Tan RQ, Cui P, Song WJ (2009) *J Sol-Gel Sci Technol* 51:198
19. Serier H, Gaudon M, Ménétrier M (2009) *Solid State Sci* 11:1192
20. Zhao J, Tan R, Zhang Y, Yang Y, Guo Y, Zhang X, Wang W, Song W (2011) *J Am Ceram Soc* 94:725–728
21. Stubhan T, Salinas M, Ebel A, Krebs FC, Hirsch A, Halik M, Brabec CJ (2012) *Adv Energy Mater* 2:532
22. Zhang H, Stubhan T, Li N, Turbiez M, Matt GJ, Ameri T, Brabec CJ (2014) *J Mater Chem A* 2:18917
23. Min J, Luponosov YN, Ameri T, Elschner A, Peregodova SM, Baran D, Heumüller T, Li N, Machui F, Ponomarenko S, Brabec CJ (2013) *Org Electron* 14:219–229
24. Scherf U, Gutacker A, Koenen N (2008) *Acc Chem Res* 41:1086–1097
25. Seo JH, Gutacker A, Sun Y, Wu H, Huang F, Cao Y, Scherf U, Heeger AJ, Bazan GC (2011) *J Am Chem Soc* 133:8416
26. He ZC, Zhong CM, Su SJ, Xu M, Wu HB, Cao Y (2012) *Nat Photonics* 6:591–595
27. Kyaw AKK, Wang DH, Gupta V, Zhang J, Chand S, Bazan GC, Heeger AJ (2013) *Adv Mater* 25:2397–2402
28. Choi H, Park JS, Jeong E, Kim G-H, Lee BR, Kim SO, Song MH, Woo HY, Kim JY (2011) *Adv Mater* 23:2759–2763
29. Jeong JK, Won Yang H, Jeong JH, Mo Y-G, Kim HD (2008) *Appl Phys Lett* 93:123508
30. Litzov I, Azimi H, Matt G, Kubis P, Stubhan T, Popov G, Brabec CJ *Org Electron* 15(2):569–576
31. Oh H, Krantz J, Stubhan T, Litzov I, Brabec CJ (2011) *Sol Energy Mater Sol Cells* 95:2194
32. Stubhan T, Oh H, Pinna L, Krantz J, Litzov I, Brabec CJ (2011) *Org Electron* 12:1539
33. Stubhan T, Ameri T, Salinas M, Krantz J, Machui F, Halik M, Brabec CJ (2011) *Appl Phys Lett* 98:253308
34. Wolf N, Rydzek M, Gerstenlauer D, Arduini-Schuster M, Manara J (2013) *Thin Solid Films* 532:60–65
35. Wolf N, Stubhan T, Manara J, Dyakonov V, Brabec CJ (2014) *Thin Solid Films* 564:213
36. Sista S, Park M-H, Hong Z, Wu Y, Hou J, Kwan WL, Li G, Yang Y (2010) *Adv Mater* 22:380